Sulfur/Nitrogen Dual-doped Porous Graphene Aerogels Enhancing Anode Performance of Lithium Ion Batteries

Hui Shan[a,b], Xifei Li[a,b,*], Yanhua Cui[c], Dongbin Xiong[a,b], Bo Yan[a,b], Dejun Li[a,b], Andrew Lushington[d], Xueliang Sun[a,b,d]

[a] Energy & Materials Engineering Centre, College of Physics and Materials Science, Tianjin Normal University, Tianjin 300387, China
[b] Tianjin International Joint Research Centre of Surface Technology for Energy Storage Materials, Tianjin 300387, China
[c] Institute of Electronic Engineering, CAEP, Mianyang 621900, China
[d] Nanomaterials and Energy Lab, Department of Mechanical and Materials Engineering, University of Western Ontario, London, Ontario N6A 5B9, Canada

A B S T R A C T

Sulfur/nitrogen dual-doped graphene aerogels (SNGAs) with a unique porous network structure have been designed through a facile and versatile one-pot hydrothermal strategy. When employed as anode in LIBs, the SNGAs with nitrogen content of 1.50 wt.% and sulfur content of 15.11 wt.% exhibit superior cycle life and rate capability. For example, a high reversible capacity of 1109.8 mAh g^{-1} can be obtained after 400 cycles even at a high current density of 800 mA g^{-1}. It was discreetly demonstrated that the prominent improved performance of SNGAs can be mainly ascribed to the effect of dual-doping heteroatoms in cooperation with each other in to the graphene lattice as well as the porous nanostructure facilitating the mass transfer for both ions and electrons. Our conclusions illustrate that the strategy of dual-doped graphene aerogel may promote the potential application of graphene for high performance lithium ion batteries.

© 2016 Elsevier Ltd. All rights reserved.

1. Introduction

As one of the most effective energy storage devices, lithium ion batteries (LIBs) have been playing an exclusive role in portable electronic devices and energy device, due to their high energy density, long cycling life as well as sustainability, providing promise energy power instead of fossil fuels [1]. Currently, the application of LIBs widely extended form mobile phones to electric vehicles (EVs) exhibiting strengthening momentum in rechargeable battery markets [2,3]. However, the graphite as an anode material of commercial LIBs possesses a relatively low theoretical specific capacity (~372 mAh g^{-1}). It is well known that increasing lithium storage capacity and enhancing rate capability are the two keys to optimize the properties of anode materials [4–6]. Graphene aerogels (GAs), a new class of ultralight and porous carbon materials, have been well-recognized by extensive investigation in the past few years. With its fascinating mechanical, thermal and electrochemical speciality, GAs have shown great potentials to optimize anode performance in LIBs [7–9]. Particularly, in view of the highly electrical conductivity with combination of 3D porous architectures, GAs can provide multidimensional electron transport pathways, increase the contact area of electrode/electrolyte, and reduce the transport distances for both ions and electrons, which can significantly improve the energy/power density of LIB system [10,11]. More importantly, heteroatom doping (such as S, N, B and P) has been demonstrated to be a pivotal strategy to optimize graphene performance due to the further enhanced electronic conductivity and Li$^+$ storage sites [12–15]. It has been reported accordingly that hole doping levels of single-layer graphene transistor can topped at to 5×10^{13} cm^{-2} [16]. Nitrogen (N) atomic has a similar size but discriminating electro negativity with carbon atomic (C: 2.55; N: 3.04). As a result, nitrogen-doped graphene (NG) has been wildly investigated and supposed to modify the graphene-based anode materials of LIBs [17,18]. As previously reported by our group, the nitrogen-doped graphene with 2.8 at.% nitrogen content as anode for LIBs displays superior electrochemical performance (684 mAh g^{-1} was retained at a current density of 100 mA g^{-1} after 500 cycles) over pristine graphene [19]. Note that the electrochemical performance of nitrogen-doped graphene

materials can be further optimized by regulating the synthetic method and/or the doped content. For instance, Cai et al. stated that the higher content (about 7.04 at.%) of nitrogen embedded in graphene via thermal annealing results in better performance [20]. However, the graphene material with single element doping inevitably confront the performance bottlenecks as a result of the limited capability of graphene to accommodate single heterogeneous atom. Therefore, the strategy of dual-doped graphene has been well documented to be a more promising way to promote the electrochemical performance of graphene [21]. It is due that the opening band-gap and the defects caused by the introduction of nitrogen and sulfur atomics endow graphene with improved electrical conductivity and promoted electrochemical reaction active sites [22,23]. The increased lithium storage performance benefits from the matching electronic structure as well as the consequent structural defects of dual-doped behavior. For example, Zhuang et al. obtained co-doped carbon materials with the elemental content of 12.36 mas.% N and 2.40 mas.% S, when conducted at 100 mA g^{-1} after 50 cycles, this materials can sustain a higher reversible capacity of 675.1 mAh g^{-1} than undoped samples [24]. Unfortunately, a direct correspondence between Li^{+} storage behavior and the remarkable contribution of dual-doping atoms has been rarely established. Therefore, there is still a great desire to develop an easy, effective, and extensible approach for refining the surface defects of graphene caused by N/S dual-doping, and illuminate the defects with relation to its electrochemical performance.

Herein, we designed three-dimensional (3D) S/N dual-doped monolithic graphene aerogels (SNGAs) via a simple and facile one-step hydrothermal method, which can precisely control the doping ratio and level of diverse heteroatoms. Additionally, compared with organic doping agent [4] and other dopants (such as, ammonium persulfate) [25,26], which may cause long-term adverse effects in the environment and high cost, thiourea as the single doping agent for sulfur/nitrogen source is little toxic to organisms. Moreover, some doping strategies inevitably consist of post-treatment at high temperature [4,25]. In this study, a simple and facile one-step hydrothermal approach was proposed to obtain S/N dual-doped porous graphene aerogels without post-treatment. The as-prepared SNGA samples possessing 3D interconnected frameworks with a porous architecture and crumpled surface are favorable for ion diffusion and electron transport. Additionally, the dual-doped of N and S atoms in graphene lattice exert characteristic synergistic effect, including more defects and advantageous electronic structure, which will promote the electrochemical performance of the graphene anode for LIBs. Our study successfully reveals the synergistic effect of dual-doping and will promote graphene materials for further applications in LIBs.

2. Experimental

2.1. Materials

Graphite powder (purity ≥ 99.95%), particle diameters of about 1.3 μm was produced from Aladdin (Shanghai, China). Other chemical reagents, such as KMnO$_4$ (99%), NaNO$_3$ (99%), concentrated sulfuric acid (95% ~ 98%), hydrochloric acid (36 ~ 38%), H$_2$O$_2$ (30%), and thiourea were supplied by Tianjin FengChuan Chemical Reagent Technology Ltd. (China). The chemicals were all analytical reagents.

2.2. Synthesis of graphene aerogel (GA) and S- and N-doped graphene aerogel (SNGA)

The synthesis of graphite oxide derived from natural graphite via a modified Hummers' method, as previously reported by our group [27]. In a typical experiment, graphene oxide (GO) aqueous suspension was obtained by ultrasonic of the resultant graphite oxide in deionized water for 30 min. Then the desirable brown dispersion was centrifuged for 30 min at 10000 rpm to remove impurities. Subsequently, different amounts of thiourea was added into the GO suspension under vigorous stirring for 30 min, the as-prepared suspension was transferred into a Teflon-lined autoclave with a 50 mL volume and maintained at 180 °C for 24 h. Then, the as-obtained product was filtered and washed by distilled water repeatedly. Finally, the products were freeze-dried to obtain SNGAs. The resultant materials synthesized by adding GO and thiourea with different ratio of 1:10, 1:20, 1:30 1:50 and 1:100 were labeled as SNGA-I, SNGA-SI, SNGA-II, SNGA-SII and SNGA-III, respectively. For comparison, the product without additive of thiourea was synthesized under the similar condition, which was labeled as GA-I.

2.3. Materials characterization

The powder XRD data was checked out by an X-ray diffractometer (D8 Advance of Bruker, Germany) with Cu/Kα radiation ranging from 5° to 85°. The Raman test of as-obtained materials was measured on a Raman Spectrometer attached LabRAM HR800 system (HORIBA, Korea) in the range of 1000 ~ 2000 cm^{-1}. Surface area measurements based on nitrogen adsorption isotherms were recorded using a surface properties analyzer instrument (ASAP 2020, Micromeritics). XPS was performed on a VG ESCALAB MK II X-ray photoelectron spectrometer. The analysis of element composition was conducted on energy dispersive X-ray spectroscopy (EDX, INCA x-sight, Oxford) and Elementar element analyzer (VARIO EI cube). The morphologies of the samples were verified using field-emission scanning

○ C ● O ● N ● S • H
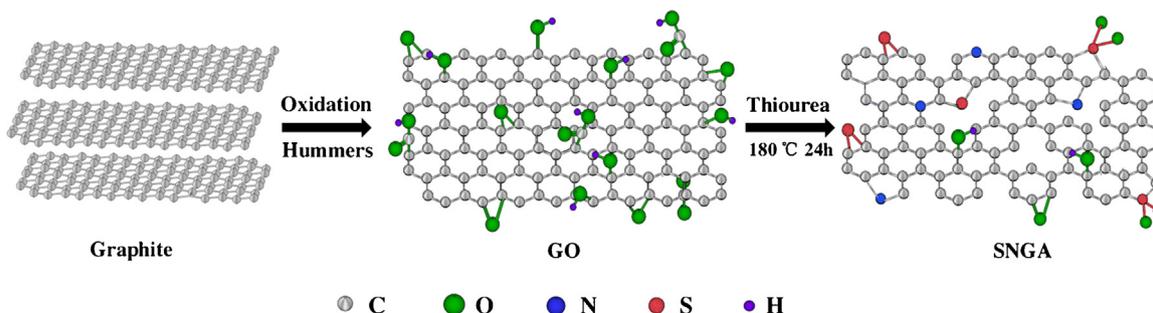
Scheme 1. Schematic design of S/N dual-doped GAs.

electron microscopy (FE-SEM, SU8010, Hitachi) and high-resolution transmission electron microscopy (HR-TEM, JEM-3000F).

2.4. Electrochemical characterization

The lithium storage performance of as-obtained samples was investigated utilizing CR2032 coin-type cells. The manufacture of working electrode was by mixing active material (GA or SNGA), acetylene black (Super-P) and polyvinylidenefluoride (PVDF) binder according to the ratio of 8:1:1 in N-methyl-2-pyrrolidinone (NMP). The amount of the active material of each electrode is about $2.83\,mg\,cm^{-1}$ averagely. Then the mixture was subsequently coated on the copper foil following the dry process in a vacuum at $90\,^\circ C$ for 12 h. The assembling of coin cells were in a glove box filled with high purity argon, using pure lithium as counter electrode and reference electrode, 1 M $LiPF_6$ dissolved in a solution containing dimethyl carbonate and ethylene carbonate with a weight ratio of 1:1 by volume as electrolyte. Cyclic voltammograms (CV) were performed using a electrochemical workstation (Princeton Applied Research Versa STAT 4) at a scan rate of $0.1\,mV\,s^{-1}$ within the voltage range of $0.01\sim3.0\,V$ (vs. Li/Li$^+$). The electrode performance was measured by the galvanostatic discharge-charge method in a voltage range between 0.01 and 3.0 V (vs. Li/Li$^+$) with the battery test system (LANHE CT2001A). Electrochemical impedance spectroscopy (EIS) data was obtained by Princeton Applied Research (Versa STAT 4) at a frequency from 0.01 Hz to 100 kHz with the AC amplitude of 5.0 mV.

3. Results and Discussion

Scheme 1 illustrates the synthesis procedure of SNGA. Abundant oxygenic functional groups were introduced during the oxidation process of graphite. Then, S/N dual-doped GAs were obtained via one-step hydrothermal reaction with GO and thiourea. Various doping species of both nitrogen and sulfur atoms were formed, as shown in Scheme 1, *viz.*, the incorporated atoms located in the vacancies and edge sites of graphene lattice, which were defined as pyridinic-N, pyrrolic-N, graphite-N, Sulfur, thiophene-S, and sulfate-S. By controlling the mass ratio of thiourea and GO, several typical samples with different content of crucial pyridinic-N and sulfated-S were fabricated.

The 3D morphology of as-prepared GA-I and SNGA samples were confirmed in Fig. 1. An interconnected framework of graphene nanosheets with porous structure can be discerned in all the samples. GA-I features the appearance of ultrathin and continuous macropores but with partial agglomeration (Fig. 1a), which is similar to the previous reports[24,28]. After GO hydrothermal reaction with thiourea, SNGA samples reveal a porous interconnect network consisting of stacked graphene sheets (Fig. 1b, 1c and 1d). The introduction of different amount of heteroatoms does not obviously affect the crumpled-like surface and three dimension structure of SNGA, which will contribute to the facile access of electrolytes and efficient transfer of lithium ions and electrons.

The morphology and microstructure of the as-prepared GA and SNGA can be further confirmed by TEM. Fig. 2 shows the TEM images of all the desired materials. Specifically, GA displays
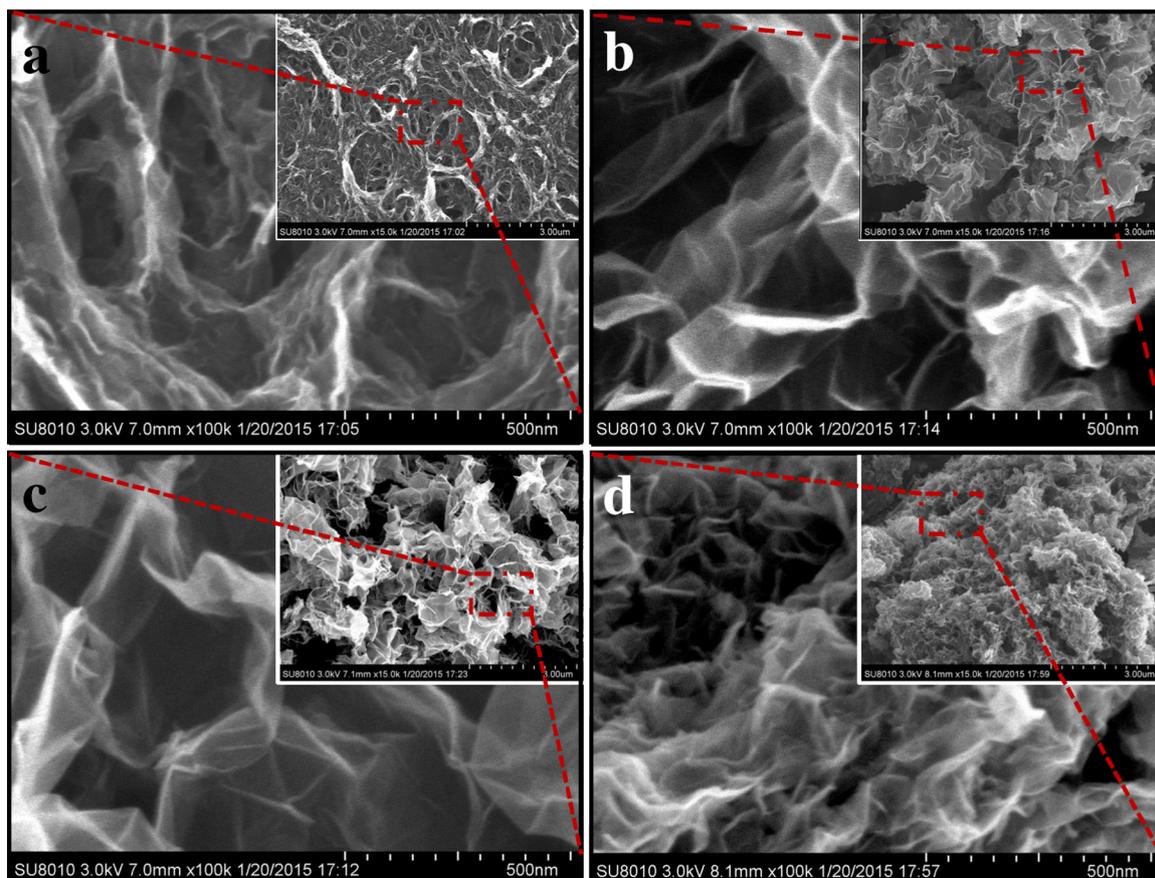
Fig. 1. SEM images of GA- I (a), SNGA- I (b), SNGA- II (c) and SNGA-III (d).
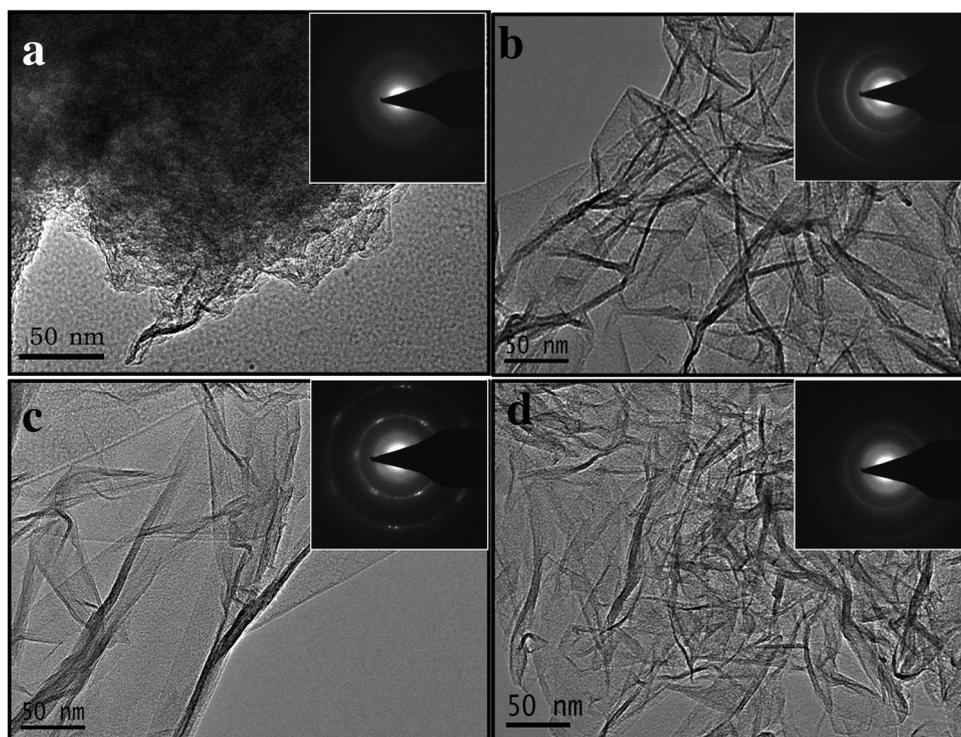
Fig. 2. TEM images of GA- I (a), SNGA- I (b), SNGA- II (c) and SNGA-III (d), the inset is the SAED patterns.

multilayered structure with agglomeration due to the van der Waals interactions and π-π stacking [9]. Clearly, the SNGA samples in Fig. 2b–d present typical voile-like structure with corrugations and scrolling. They maintain the porous structure and exhibit even thinner and more transparent layers. As shown in Fig. S1, the high resolution TEM image (HRTEM) shows that the amorphous carbon material was formed by the stacking of the curved graphene layers, featuring a multi-layer porous structure. With the successfully doping of S and N atoms, the binding bonds between C and S or N was developed definitely. The selected area electron diffraction (SAED) patterns shown in the inset of each picture display a typical ring feature. The SAED patterns of SNGA reveal well-defined polycrystalline diffraction ring, suggesting the enhanced graphitic degree of SNGA as a result of S/N dual- doping [29].

X-ray photoelectron spectroscopy (XPS) was conducted to investigate the states of elements in as-prepared samples. As shown in Fig. 3a, two characteristic peaks located at 532 and 285 eV were observed in the survey spectra of all the samples, corresponding to O 1s and C 1s spectrum, respectively [30]. Another two visible peaks located at 163 and 400 eV were found in three SNGA samples, which result from S 2p and N 1s, respectively [4,31]. In particular, Fig. 3b enlarges N 1s and S 2p peaks of SNGA-II, which indicates the co-existence of S and N. As shown in Table S1, the percentage of doped sulphur into SNGA-I, SNGA-II and SNGA-III was estimated to be 2.10, 2.09 and 2.76 at.%, while 0.72, 1.15 and 1.21 at.% for nitrogen doping, respectively. The C/O ratios of GA-I, SNGA-I, SNGA-II and SNGA-III were 8.08, 10.39, 9.98 and 11.12, respectively. On one hand, lower oxygen ratio indicates higher electrical conductivity [32]. On the other hand, as previously reported by our group [33], surface oxygen-containing functional groups function as some electrochemical active sites. As a result, the C/O ratio shows optimized value to exhibit better rate capability. Summarily, the large doses of dopant result in high doping level of heteroatoms.

The high resolution spectra of C 1s, S 2p, N 1s and O 1s in SNGA-II can be resolved into several peaks. The sharp C 1s peak (Fig. 3c) is decomposed into three components centered at 284.6 (C-C/C-N), 285.6 (C-S/C-N), and 288.0 eV (O—C=O) [4]. The O 1s (Fig. 3d) peak can be resolved into four peaks with binding energies of 530.6 (O-S) [34], 532.5 (C-OH), 533.4 (HO—C=O) and 536.0 eV (H_2O) [3]. The S 2p peak can be disassembled into three peaks at 164.0 (Sulfur), 165.3 (Thiophene S), and 168.8 eV (Sulfate) (Fig. 3e) [35,36]. The N 1s peak can be disintegrated into three peaks at 398.5 (Pyridinic N), 400.2 (Pyrrolic N), and 401.2 eV (Graphite N) (Fig. 3f) [37]. The high resolution spectra of S 2p and N 1s in SNGA-I and SNGA-III are revealed in Fig. S2. These observations indicate that both sulfur and nitrogen atoms are in three different bonding states in the doped GAs. In addition, the low peak at 536.0 eV may be attributed to the chemisorbed oxygen or free hydrone on carbon surfaces. The numeric results of their contents are summarized in Table 1, and the corresponding structure model is given in Scheme 1. It can be seen that in all three SNGA samples, N and S contents are as order: pyrrolic-N > pyridinic-N > graphitic-N, and Sulfur > Thiophene S > sulfate, respectively. Furtherly, using elemental element analyzer, the formation of SNGA-I, SNGA-II and SNGA-III was established in Table 2. One can see that the SNGA-III has the highest nitrogen (2.76 wt.%) and sulfur concentration (20.26 wt.%), and its sulfur concentration differs from the value of XPS (2.76 at.%) shown in Table S1. It may be due that XPS is surface phenomenon. Both XPS and elemental analysis confirm the introduction of N and S atoms into graphene lattice.

The XRD patterns of GA-I, SNGA-I, SNGA-II and SNGA-III are compared in Fig. 4a. For comparison, the XRD patterns of nature graphite and GO are shown in Fig. S3. The strong and sharp peak positioned at 26.6° indicates regular space arrangement of the natural graphite, relating to the interlayer spacing of about 0.34 nm. After chemical oxidation, the graphite is oxidized into GO, and the graphitic structure is partial broken. A typical diffraction peak at 2θ = 11.8° of GO is observed, which could be assigned to the (002) reflection, corresponding to an increased interlayer spacing of about 0.749 nm. It is due to the introduction of abundant oxygenic functional groups such as —O—, —OH and
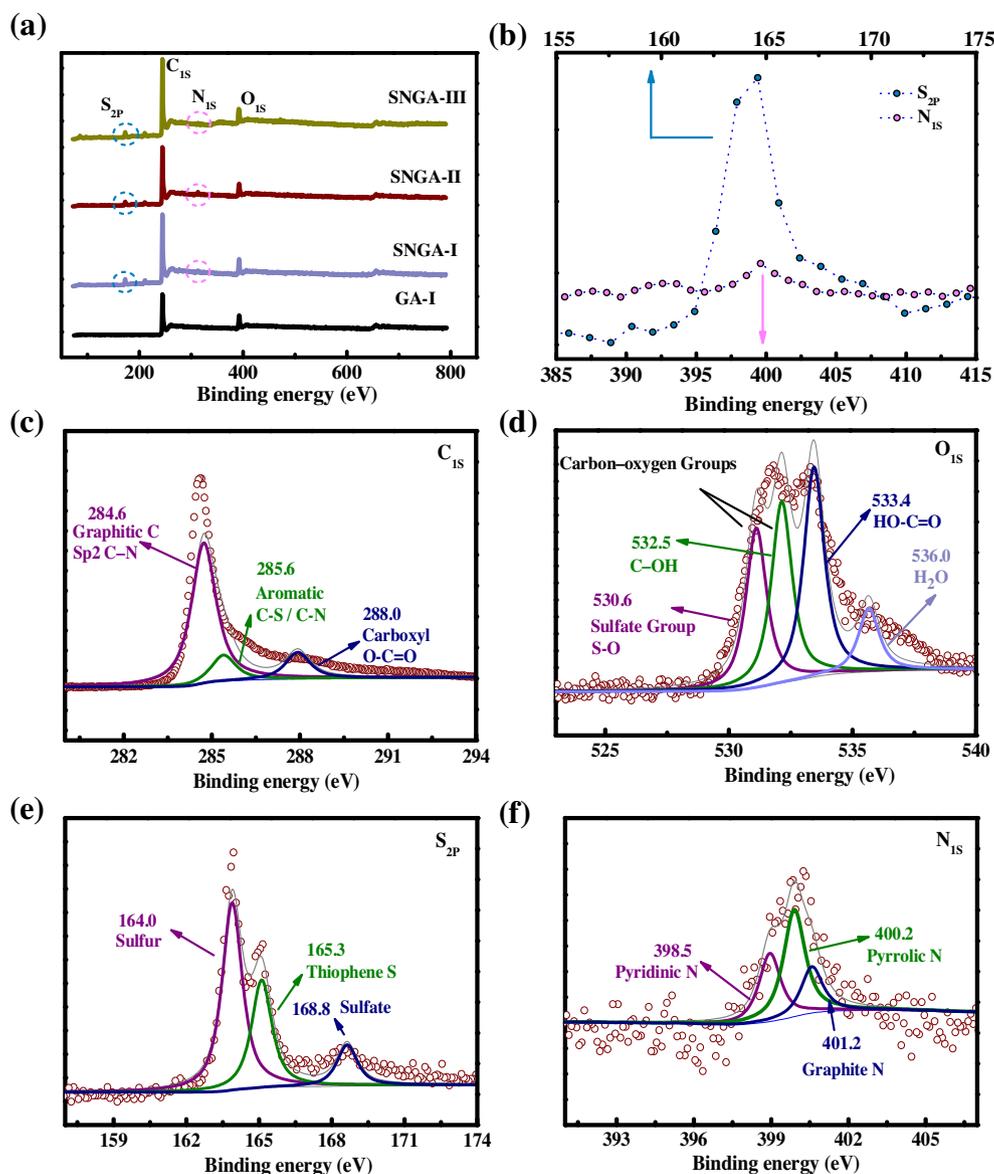
Fig. 3. (a) XPS survey spectra of GA- I, SNGA- I, SNGA- II and SNGA-III; (b) Local enlarge spectra of the N 1s and S 2p peaks of SNGA- II; The typical C 1s (c), O 1s (d), S 2p (e) and N 1s (f) XPS spectra of SNGA-II.

Table 1
S and N species content (at.%) of the samples based on XPS results.

Samples	S			N		
	Sulfur	Thiophene	Sulfate	Pyridinic	Pyrrolic	Graphite
SNGA-I	61.7	30.10	8.17	27.35	50.71	21.94
SNGA-II	44.66	29.83	25.51	33.34	49.09	17.57
SNGA-III	63.31	31.65	5.04	24.99	53.27	21.74

—COOH as well as absorbed H_2O molecules[33,38]. After hydrothermal treatment for 24 h, the oxygenic functional groups and interlayer water of GO were greatly released, resulting in decreasing interlayer spacing[39]. As shown in Fig. 4a, all samples have two observed diffraction peaks around $2\theta = 24°$ and $43°$, which can be indexed as the (002) and (100) plane, respectively. The (002) plane is in accordance with the interlamellar distance of

0.38 nm. It's worth noting that all SNGA samples present the weaker and wilder diffraction peaks compared with that of GA-I. It is ascribed to the decreased size of graphene layers and increased disorder degree.

Raman was carried out to examine defects and imperfections of as-obtained samples. As shown in Fig. 4b, two distinct peaks at about 1360 and 1580 cm^{-1} were observed, in accord with D and G

Table 2
Elemental analysis (wt.%) of SNGA-I, SNGA-II and SNGA-III.

| Sample	C	H	N	S	O
SNGA-I	78.75	0.49	0.91	11.88	7.97
SNGA-II	68.18	1.09	1.5	15.11	14.12
SNGA-III	55.6	5.42	2.76	20.26	27.16

band, respectively. The D band results from the defects or structural disorder in carbon based materials; whereas the G band roots in sp^2 bonded ordered graphitic carbon. The intensity ratio of the G to D band (I_D/I_G) is generally used to evaluate the level of the structural disorder [38,40,41]. Compared the ratio (I_D/I_G) of GO and SNGA-II, there is a significant disparities. Obviously, the doped graphene shows higher values of I_D/I_G 1.53 than the pristine one with 1.28, indicating that more structural defects and edge plane exposure result from the introduction of S and N into graphene layers.

Nitrogen adsorption/desorption tests were performed to further confirm the texture properties of the as-obtained graphene aerogels, as shown in Fig. 4c and d. A typical characteristic hysteresis loop ($P/P_0 = 0.40$) was found in the N_2 adsorption–desorption isotherms of the SNGA-II samples, featuring a superior mesoporous property [24]. The BET surface area of the GA-I was estimated to be 593.28 $m^2 g^{-1}$, and the pore size of approximately 2.77 nm was determined based on the BJH adsorption curve. With the introduction of S and N, the specific surface area of SNGA-II was increased up to 624.48 $m^2 g^{-1}$, and the pore size was 4.93 nm. Additionally, the pores of GA-I were distributed in the range of 2–8 nm. After S/N impregnation, most pore sizes are increased into the scale of 3–30 nm (see the inset of Fig. 4c and 4d) By contrast, SNGA-II reveals more mesoporous characteristic, which is beneficial for the Li diffusion and reducing the energy barrier of diffusion.

Fig. 5 shows the cyclic voltammetry (CV) profiles of the obtained GA and SNGA electrodes in the initial 3 cycles at a scan rate of 0.1 mV s^{-1} in the voltage range of 0.01 to 3.0 V (vs. Li/Li$^+$). In the first cycle of GAs (Fig. 5a), a reduction peak located at 0.58 V was observed, and then disappeared in the subsequent cycles. It is attributed to the decomposition of the electrolyte and the formation of solid electrolyte interface (SEI) film on the electrode surface [42]. Differing from GAs, as shown in Fig. 5, the peak at ∼2.05 V could be attributed to the transition of S to polysulfides. In the relevant oxidation process, the peak located at 2.4 V corresponds to the transformation of Li$_x$S into the polysulfides [43]. In addition, a pair of redox peaks located at 1.6 V/1.9 V can be attributed to the sulfur embedded in the pores of SNGAs (Li insertion) and the opposite behavior (Li extraction) [44].

Fig. 6a–d compare the charge–discharge curves of the GA-I, SNGA-I, SNGA-II and SNGA-III electrodes in the 1st, 2nd, 10th, 20th, 50th and 100th cycles. The first cycle discharge/charge capacities of the GA-I, SNGA-I, SNGA-II and SNGA-III electrodes were 1628.7/920.2, 1207.2/917.3, 1523.7/981.4, 1483.1/780.7 mAh g^{-1}, respectively. Meanwhile, the coulombic efficiency (CE) for all the electrodes (Fig. S4) is 56.50%, 75.99%, 64.41% and 52.64% in sequence. For the dual-doped system, the different initial coulombic efficiency of SNGA can be attributed to the different-sized porosity and layers of the electrode materials as well as the penetration of the electrolyte in a bulk electrode. The low CE is mainly due to the irreversible lithiation behavior as a result of the formation of solid electrolyte interphase (SEI) film. Notably, S doping has two different types of contribution to the enhancement of initial coulombic efficiency. Doped S like thiophene S can increase the new active sites for Li$^+$ storage but sulfur drives down the electrical conductivity of SNGA electrode materials (see Fig. 7d). Based on the value of elemental analysis, SNGA-III delivered a lowest coulombic efficiency resulted from the abundance of elemental sulfur [45]. It is well known that the electrochemical reaction of sulfur with lithium is a multi-step process, and it exhibits two potential plateaus around 2.5 and 2.0 V vs. Li$^+$/Li, respectively. For our dual-doped samples, the cathodic
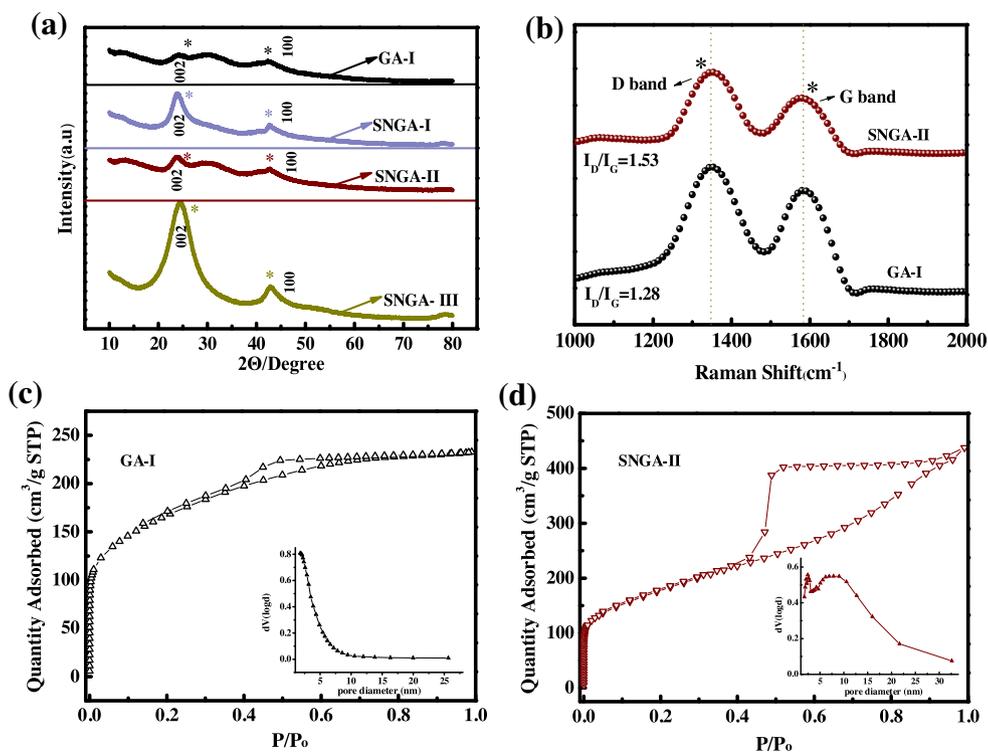
Fig. 4. (a) XRD patterns of GA- I, SNGA- I, SNGA- II and SNGA-III; (b) Raman spectra of GA- I and SNGA- II; Nitrogen adsorption/desorption isotherms of GA-I (c) and SNGA-II (d) (inset: the pore size distribution).
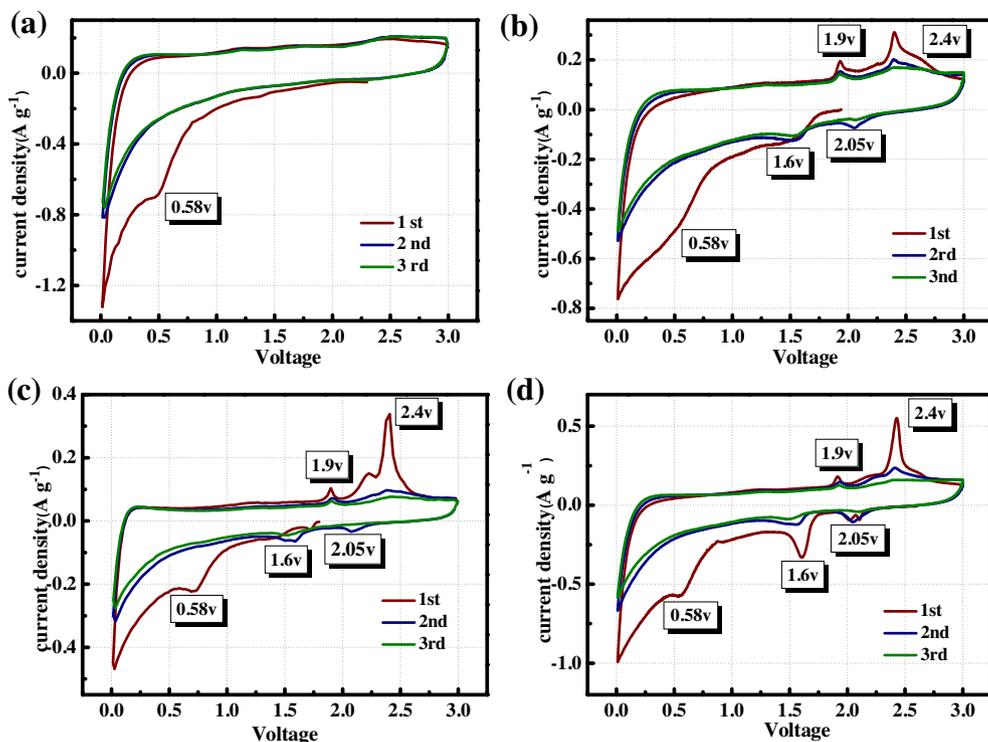
Fig. 5. Cyclic voltammograms of (a) GA-I, (b) SNGA-I, (c) SNGA-II and (d) SNGA-III in the voltage range of 0.01 ∼3.0 V (vs. Li/Li⁺) at a scan rate of 0.1 mV s⁻¹.

potential plateaus at around 1.80 V suggested the reaction of S and lithium to form Li_xS. In the opposite anodic process, the potential plateaus at 2.4 V implied the staged reversible transitions between

Li_xS and high-order polysulfides. After the initial cycle, the plateaus disappeared which were observed in the charge-discharge profiles. This phenomenon can be attributed to the dissolution loss of S into
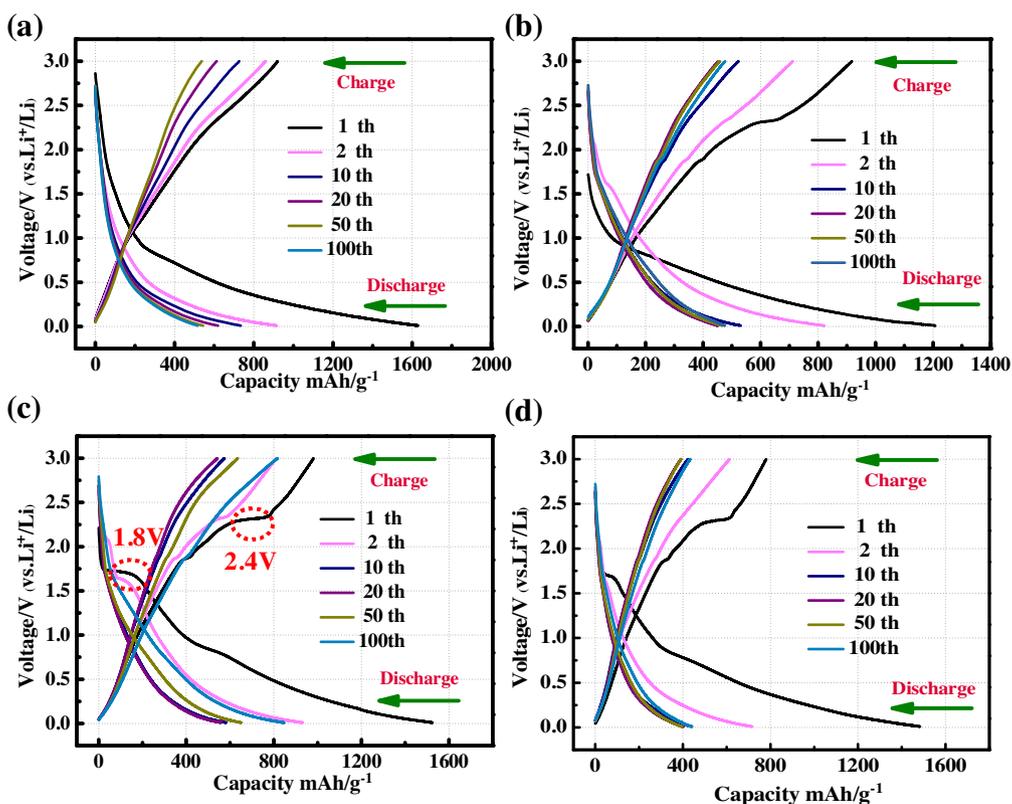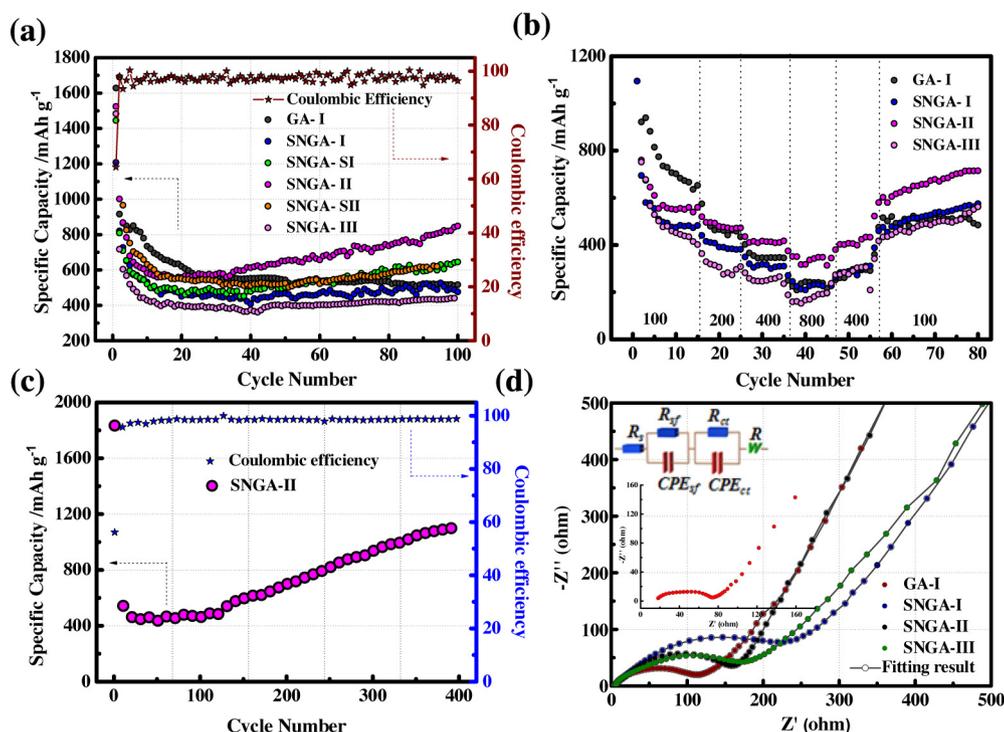

Fig. 6. Galvanostatic discharge-charge profiles of (a) GA-I, (b) SNGA-I, (c) SNGA-II and (d) SNGA-III at the current density of 100 mA g⁻¹ in the voltage range of 0.01 ∼3.0 V (vs. Li/Li⁺).

Fig. 7. (a) Cycling performance of GA-I, SNGA-I, SNGA-SI, SNGA-II, SNGA-SII and SNGA-III at the current density of 100 mA g^{-1} and the coulombic efficiency of the SNGA-II; (b) Rate performance of GA-I, SNGA-I, SNGA-II and SNGA-III at various current densities; (c) Cycling performance of SNGA-II at the current density of 800 mA g^{-1}; (d) Nyquist plots of GA-I, SNGA-I, SNGA-II and SNGA-III after 10 cycles at a charge state (3.0 V) and the simulated results (inset: the equivalent circuit used to simulate an experimental curve and the Nyquist plots of SNGA-II after 265 cycles).

the electrolyte, causing capacity fade. Simultaneously, with the formation of initial phase, co-contribution for all kinds of sites function less for Li$^+$ storage which prompted the irreversible process but re-activated later. In view of the full contact of electrode and electrolyte, the capacity increased upon subsequent cycling.

Fig. 7a compares the cycling response of GA-I, SNGA-I, SNGA-SI, SNGA-II, SNGA-SII, and SNGA-III electrodes in the initial 100 cycles at a current density of 100 mA g^{-1}. The reversible capacities of all electrodes sharply decrease in the first few cycles. As previously reported, this phenomenon usually occur in graphene-based anodes, which could be attributed to the inevitable formation of the SEI layer caused by electrolyte decomposition and the irreversible reaction of the lithium ion with the in-plane graphitic sites [6,46,47]. After 100 charge/discharge cycles, GA-I revealed the discharge capacity of 516.6 mAh g^{-1}, while the discharge capacities of SNGA-I, SNGA-II, SNGA-III, SNGA-SI and SNGA-SII were 475.6, 847.8, 440.9, 644.9 and 632.4 mAh g^{-1}, respectively. The superior cycle performance of SNGA-II can be attributed to the enhanced conductivity confirmed by electrochemical impedance spectroscopy in Fig. 7d. Moreover, SNGA-III with the inferior cycle performance reveals the highest S concentration (~20.26 wt.%), which include 63.31 at.% sulfur confirmed by XPS. Due to the low electronic conductivity of S, a large number of sulfur not only lower the conductivity of SNGA-III, but also reduce the proportion of active materials in the SNGAs electrode. More surprisingly, the discharge capacity of SNGA-II gradually increases up to 1822.8 mAh g^{-1} after 265 cycles at the current density of 100 mA g^{-1} (see Fig. S5). Numerically, in SNGA-II which reveals superior electrochemical performance, the sum of the pyridinic N (33.34 at. %) and sulfate (25.51 at.%) maintained dominant. It is documented that the pyridinic N possesses a localized density of states in the occupied region near the Fermi level (20), and the carbon atoms can behave as Lewis bases owing to the possibility of electron pair

donation. Actually, the electrochemical active sites are related to the carbon atoms next to the pyridinic N rather than pyridinic N themselves [48]. This mechanism can be also suitable to heteroatom S. Notably, similiar to pyridinic N, the sulfur atoms in sulfate is another electron-deficient element, which can stimulate more conjoint carbon atoms as active sites for Li$^+$ storage. By contrast, thiophene (similar to pyrrolic-N) is defined as an electron-rich system which has a weaker acceptance capability of electrons. Therefore, the carbon atoms next to pyridinic N and sulfate S with Lewis basicity play an important role as more electrochemical active sites for facilitating electron transport and lithium ion diffusion. In addition, Denis et al. reported that S doping can induce different effects: the doped sheet can be a small-band-gap semiconductor at a low S concentration (2 atom%), or it can have better metallic properties than the pristine sheet at a higher S concentration (4 at.%, a graphene sheet doped by two S atoms) [49]. During the doping process, different types of nitrogen and sulfur precursors were initially mixed into the graphene oxide, and S/N dual-doping was achieved accompanied by the reduction of graphene oxide via a hydrothermal reaction. With the introduction of S and N, pyridinic N and sulfate S stimulate the conjoint carbon atoms as active sites for Li$^+$ storage as well as prompting the formation of porous structure to further optimize the electrochemical performance of SNGA electrodes. However, in particularly, some carbon atoms adjacent to the pyridinic N and sulfate S gradually reacted with oxygen containing functional groups, which resulted in the transition of pyridinic N to pyridonic N [48]. Some electrochemical active sites disabled, causing inevitable capacity fade. After 30 cycles, the noteworthy is the reversible capacity of SNGA-II broken to grow up. The increased capacity for doped graphene can be mainly attributed to several reasons: (i) the reversal of carbon atoms and re-activation of pyridinic N and sulfate S, providing more active sites for lithium storage [50]; (ii) the proliferation of in-plane defects during the

electrochemical cycling; (iii) gradual penetration of electrolyte into the porous structure, promoting the activation of electrode materials [51]; (iv) the synergistic effects of N and S co-doping in graphene [8].

To further confirm the performance improvement, the rate capacity of GA-I, SNGA-I, SNGA-II and SNGA-III electrodes at various current densities of 100, 200, 400 and 800 mA g^{-1} was studied in Fig. 7b. At each current density, SNGA-II delivers higher rate capability than other anode materials. In particular, when the current density was reset back to 200 and 100 mA g^{-1}, all the electrode resumes the reversible capacity, moreover, SNGA-II performs the best. Additionally, the SNGA-II electrode was tested at a high current density of 800 mA g^{-1}. As shown in Fig. 7c, the specific capacities increased up to 1109.8 mAh g^{-1} after 400 cycles, and the coulombic efficiency approximated to almost 100%, which further indicates the superior lithium storage performance and outstanding cycling stability of the designed dual-doped GA anode material.

In recent years, graphene-based electrode materials have attracted tremendous attention due to superior electrical conductivity and high contact area with electrolyte. However, some geometrical and electrochemical nonequivalent lithium storage sites of the graphene anode materials cause the absence of the plateaus during charge/discharge processes [52], as shown in Fig. 6 and Fig. S6. It is an important disadvantage of graphene anode materials. In addition, in this study, the voltage was in the range of 0.01 ~ 3.0 V to clearly highlight obvious effects of S/N dual-doping behavior on electrochemical performance of anode materials. As for anode materials, the voltage range should be as low (such as 0.01 ~ 1.0 V) as possible to increase the output voltage and the energy density for a full battery. One can see in Fig. S6 that in the voltage range of 0.01 ~ 1.0 V, lithium storage capacity of graphene may be even less than graphite. But both are not our focus of this study. We mainly discerned significant impacts of S/N dual-doping behavior on anode performance. Our results clearly demonstrate important functions of dual doping in enhancing electrochemical performance of anode materials (Figs. 5 and 6, and Fig. S7), which provides a possible strategy to improve commercialized anode materials for LIBs.

The Nyquist plots of GA-I, SNGA-I, SNGA-II and SNGA-III electrodes at a charge state (2.5 V vs. Li$^+$/Li) after 10 cycles are compared in Fig. 7d. The impedance data analyzed by fitting the Nyquist plots via the equivalent circuit was shown inset [53]. The circuit consists of ohmic resistance (R_s), two RC parallel elements in series describing the SEI film on the surface (R_{sf} and CPE$_{sf}$), lithium ion charge transfer at interface (R_{ct} and CPE$_{ct}$), and Warburg impedance for solid state diffusion of lithium ions. A constant phase element (CPE) was used in the equivalent circuit instead of a pure capacitance due to the inhomogeneous surface of the thin film working electrode. CPE$_{sf}$ and CPE$_{ct}$ are constant phase elements corresponding to the surface film and double layer capacitance, respectively. According to the fitting results presented in Table 3, SNGA-II displays the lowest charge-transfer resistance (131.9 Ω), which supports the prominent electrochemistry performance over other materials. Furthermore, as shown in the inset of

Fig. 7d, the Nyquist plots of SNGA-II after 265 cycles exhibited a smaller value of 49.7 Ω for R_{ct}. It indicated that S/N co-doping significantly enhanced the electrochemical reaction activity of Li$^+$ storage, and effectively decreased the electrochemical reaction polarization of the anode material. Therefore, the electrochemical performance of the SNGA-II confirms, as has been proposed in this study, that the dual-doping of 15.11 wt.% S and 1.50 wt.% N contributes to enhance electrochemical performance. In addition, the three-dimensional porous network of SNGA provides some channels for electron transport and lithium ion diffusion with enhanced rate capability.

4. Conclusion

In summary, S/N dual-doped GAs with a unique three dimension porous frameworks have been successfully designed via a facile hydrothermal approach. When employed as anode of LIBs, the porous dual-doped framework exhibited excellent performance in terms of high reversible capacity, superior rate capacity and long-running cycle performance. The enhanced performance may be attributed to the synergistic effects of S/N dual-doped in the graphene lattice as well as the defects such as vacancies and edge sites, notably detailed for the reversal of carbon atoms and re-activation of sulfate-S and pyridinic-N which provide more active sites for lithium storage. It is believed that the designed S/N dual-doped GAs hold great promise as durable anode materials in LIBs, and thus open a new strategy to develop graphene based materials for LIBs.

Appendix A. Supplementary data

Supplementary data associated with this article can be found, in the online version, at http://dx.doi.org/10.1016/j.electacta.2016.04.105.

Table 3
The typical fitted parameters in the electrochemical impedance spectroscopy.

Sample	GA-I	SNGA-I	SNGA-II	SNGA-II[*]	SNGA-III
R_s	4.145	4.133	3.786	15.77	4.524
R_{sf}	28.41	12.63	22.5	11.86	11.74
R_{ct}	91.68	250.6	131.9	49.67	184.6

[*] The Nyquist plots of SNGA-II after 265 cycles.

References

[1] B. Dunn, H. Kamath, J.M. Tarascon, Electrical energy storage for the grid: a battery of choices, Science 334 (2011) 928–935.
[2] Y. Xu, Z. Lin, X. Zhong, B. Papandrea, Y. Huang, X. Duan, Solvated Graphene Frameworks as High-Performance Anodes for Lithium-Ion Batteries, Angew. Chem. Int. Ed. Engl. 54 (2015) 1–7.
[3] Q. Li, N. Mahmood, J. Zhu, Y. Hou, S. Sun, Graphene and its composites with nanoparticles for electrochemical energy applications, Nano Today 9 (2014) 668–683.
[4] W. Ai, Z. Luo, J. Jiang, J. Zhu, Z. Du, Z. Fan, L. Xie, H. Zhang, W. Huang, T. Yu, Nitrogen and sulfur codoped graphene: multifunctional electrode materials for high-performance li-ion batteries and oxygen reduction reaction, Adv. Mater. 26 (2014) 6186–6192.
[5] Y. Yan, Y.X. Yin, S. Xin, Y.G. Guo, L.J. Wan, Ionothermal synthesis of sulfur-doped porous carbons hybridized with graphene as superior anode materials for lithium-ion batteries, Chem. Commun. (Camb.) 48 (2012) 10663–10665.
[6] C.H. Wu, N.W. Pu, P.J. Wu, Y.Y. Peng, C.N. Shih, C.Y. Chen, Y.M. Liu, M.D. Ger, Performance improvement of lithium ion batteries using magnetite–graphene

nanocomposite anode materials synthesized by a microwave-assisted method, Microelectron. Eng. 138 (2015) 47–51.

[7] L. Jiang, Z. Fan, Design of advanced porous graphene materials: from graphene nanomesh to 3D architectures, Nanoscale 6 (2014) 1922–1945.

[8] Y. Su, Y. Zhang, X. Zhuang, S. Li, D. Wu, F. Zhang, X. Feng, Low-temperature synthesis of nitrogen/sulfur co-doped three-dimensional graphene frameworks as efficient metal-free electrocatalyst for oxygen reduction reaction, Carbon 62 (2013) 296–301.

[9] W. Ai, Z.Z. Du, J.Q. Liu, F. Zhao, M.D. Yi, L.H. Xie, N.E. Shi, Y.W. Ma, Y. Qian, Q.L. Fan, T. Yu, W. Huang, Formation of graphene oxide gel via the π-stacked supramolecular self-assembly, RSC Adv. 2 (2012) 12204.

[10] L. Lin, X. Zheng, S. Zhang, D.A. Allwood, Surface Energy Engineering in the Solvothermal Deoxidation of Graphene Oxide, Adv. Mater. Interface 1 (2014) 1300078.

[11] H. Wang, H. Feng, J. Li, Graphene and graphene-like layered transition metal dichalcogenides in energy conversion and storage, Small 10 (2014) 2165–2181.

[12] Z. Yu, J. Song, M.L. Gordin, R. Yi, D. Tang, D. Wang, Phosphorus-Graphene Nanosheet Hybrids as Lithium-Ion Anode with Exceptional High-Temperature Cycling Stability, Adv. Sci. 2 (2015) 1400020.

[13] H. Wang, C. Ma, X. Yang, T. Han, Z. Tao, Y. Song, Z. Liu, Q. Guo, L. Liu, Fabrication of boron-doped carbon fibers by the decomposition of B4C and its excellent rate performance as an anode material for lithium-ion batteries, Solid State Sci. 41 (2015) 36–42.

[14] X. Wang, Q. Weng, X. Liu, X. Wang, D.M. Tang, W. Tian, C. Zhang, W. Yi, D. Liu, Y. Bando, D. Golberg, Atomistic origins of high rate capability and capacity of N-doped graphene for lithium storage, Nano Lett. 14 (2014) 1164–1171.

[15] Y.S. Yun, V.D. Le, H. Kim, S.J. Chang, S.J. Baek, S. Park, B.H. Kim, Y.H. Kim, K. Kang, H.J. Jin, Effects of sulfur doping on graphene-based nanosheets for use as anode materials in lithium-ion batteries, J. Power Sources 262 (2014) 79–85.

[16] L.S. Panchakarla, K.S. Subrahmanyam, S.K. Saha, A. Govindaraj, H.R. Krishnamurthy, U.V. Waghmare, C.N.R. Rao, Synthesis, Structure, and Properties of Boron- and Nitrogen-Doped Graphene, Adv. Mater. (2009) 4726–4730.

[17] Z. Yang, Z. Yao, G. Li, G. Fang, H. Nie, Z. Liu, X. Zhou, X. Chen, S. Huang, Sulfur-Doped, Graphene as an Efficient Metal-free Cathode Catalyst for Oxygen Reduction, ACS Nano 6 (2012) 205–211.

[18] D. Li, H. Chen, G. Liu, M. Wei, L.-x. Ding, S. Wang, H. Wang, Porous nitrogen doped carbon sphere as high performance anode of sodium-ion battery, Carbon 94 (2015) 888–894.

[19] X. Li, D. Geng, Y. Zhang, X. Meng, R. Li, X. Sun, Superior cycle stability of nitrogen-doped graphene nanosheets as anodes for lithium ion batteries, Electrochem. Commun. 13 (2011) 822–825.

[20] D. Cai, S. Wang, P. Lian, X. Zhu, D. Li, W. Yang, H. Wang, Superhigh capacity and rate capability of high-level nitrogen-doped graphene sheets as anode materials for lithium-ion batteries, Electrochim. Acta. 90 (2013) 492–497.

[21] X. Ma, G. Ning, Y. Sun, Y. Pu, J. Gao, High capacity Li storage in sulfur and nitrogen dual-doped graphene networks, Carbon 79 (2014) 310–320.

[22] L.B. Xing, S.F. Hou, J.L. Zhang, J. Zhou, Z. Li, W. Si, S. Zhuo, A facile preparation of three dimensional N, S co-doped graphene hydrogels with thiocarbohydrazide for electrode materials in supercapacitor, Mater. Lett. 147 (2015) 97–100.

[23] X. Wang, G. Sun, P. Routh, D.H. Kim, W. Huang, P. Chen, Heteroatom-doped graphene materials: syntheses, properties and applications, Chem. Soc. Rev. 43 (2014) 7067–7098.

[24] G.l. Zhuang, J.Q. Bai, X.Y. Tao, J.M. Luo, X.D. Wang, Y.F. Gao, X. Zhong, X.N. Li, J.G. Wang, Synergistic effect of S, N-co-doped mesoporous carbon materials with high performance for oxygen-reduction reaction and Li-ion batteries, J. Mater. Chem. A 3 (2015) 20244–20253.

[25] D. Sun, J. Yang, X. Yan, Hierarchically porous and nitrogen, sulfur-codoped graphene-like microspheres as a high capacity anode for lithium ion batteries, Chem. Commun. (Camb.) 51 (2015) (2015) 2134–2137.

[26] Z. Tian, J. Li, G. Zhu, J. Lu, Y. Wang, Z. Shi, C. Xu, Facile synthesis of highly conductive sulfur-doped reduced graphene oxide sheets, Phys. Chem. Chem. Phys. 18 (2015) 1125–1130.

[27] D. Xiong, X. Li, H. Shan, B. Yan, L. Dong, Y. Cao, D. Li, Controllable oxygenic functional groups of metal-free cathodes for high performance lithium ion batteries, J. Mater. Chem. A 3 (2015) 11376–11386.

[28] Y. Xu, K. Sheng, C. Li, G. Shi, Self-Assembled Graphene Hydrogel via a One-Step Hydrothermal Process, ACS Nano 4 (2010) 4324–4330.

[29] Z. Fan, Q. Zhao, T. Li, J. Yan, Y. Ren, J. Feng, T. Wei, Easy synthesis of porous graphene nanosheets and their use in supercapacitors, Carbon 50 (2012) 1699–1703.

[30] H.R. Byon, B.M. Gallant, S.W. Lee, Y. Shao-Horn, Role of Oxygen Functional Groups in Carbon Nanotube/Graphene Freestanding Electrodes for High Performance Lithium Batteries, Adv. Funct. Mater. 23 (2013) 1037–1045.

[31] J. Liang, Y. Jiao, M. Jaroniec, S.Z. Qiao, Sulfur and nitrogen dual-doped mesoporous graphene electrocatalyst for oxygen reduction with synergistically enhanced performance, Angew. Chem. Int. Ed. Engl. 51 (2012) 11496–11500.

[32] C. Punckt, F. Muckel, S. Wolff, I.A. Aksay, C.A. Chavarin, G. Bacher, W. Mertin, The effect of degree of reduction on the electrical properties of functionalized graphene sheets, Appl. Phys. Lett. 102 (2013) 023114.

[33] D. Xiong, X. Li, H. Shan, Y. Zhao, L. Dong, H. Xu, X. Zhang, D. Li, X. Sun, Oxygen-containing Functional Groups Enhancing Electrochemical Performance of Porous Reduced Graphene Oxide Cathode in Lithium Ion Batteries, Electrochim. Acta. 174 (2015) 762–769.

[34] Z. Zhao, X. Wang, J. Qiu, J. Lin, D. Xu, C. Zhang, M. Lv, X. Yang, Three-dimensional graphene-based hydrogel/aerogel materials, Rev. Adv. Mater. Sci. 36 (2014) 137–151.

[35] S. Zhang, F. Yao, L. Yang, F. Zhang, S. Xu, Sulfur-doped mesoporous carbon from surfactant-intercalated layered double hydroxide precursor as high-performance anode nanomaterials for both Li-ion and Na-ion batteries, Carbon 93 (2015) 143–150.

[36] Yu.M. Shul'ga, V.I. Rubtsov, V.N. Vasilets, A.S. Lobach, N.G. Spitsyna, E.B. Yagubskii, EELS, XPS and IR study of C60.2S 8 compound, Synth. Met. 70 (1995) 1381–1382.

[37] F. Zheng, Y. Yang, Q. Chen, High lithium anodic performance of highly nitrogen-doped porous carbon prepared from a metal-organic framework, Nat. Commun. 5 (2014) 5261.

[38] K.S. Subrahmanyam, S.R.C. Vivekchand, A. Govindaraj, C.N.R. Rao, A study of graphenes prepared by different methods: characterization, properties and solubilization, J. Mater. Chem. 18 (2008) 1517.

[39] H.M. Ju, S.H. Huh, S.H. Choi, H.L. Lee, Structures of thermally and chemically reduced graphene, Mater. Lett. 64 (2010) 357–360.

[40] A.C. Ferrari, J.C. Meyer, V. Scardaci, C. Casiraghi, M. Lazzeri, F. Mauri, S. Piscanec, D. Jiang, K.S. Novoselov, S. Roth, A.K. Geim, Raman Spectrum of Graphene and Graphene Layers, Phys. Rev. Lett. 97 (2006) 18401.

[41] K. Krishnamoorthy, M. Veerapandian, K. Yun, S.J. Kim, The chemical and structural analysis of graphene oxide with different degrees of oxidation, Carbon 53 (2013) 38–49.

[42] X. Li, J. Liu,, Y. Zhang,, et al., High concentration nitrogen doped carbon nanotube anodes with superior Li$^+$ storage performance for lithium rechargeable battery application, J. Power Sources 197 (2012) 238–245.

[43] X. Zhou, J. Xie, J. Yang, Y. Zou, J. Tang, S. Wang, L. Ma, Q. Liao, Improving the performance of lithium–sulfur batteries by graphene coating, J. Power Sources 243 (2013) 993–1000.

[44] Y. Zhang, Y. Zhao, Z. Bakenov, M. Tuiyebayeva, A. Konarov, P. Chen, Synthesis of Hierarchical Porous Sulfur/Polypyrrole/Multiwalled Carbon Nanotube Composite Cathode for Lithium Batteries, Electrochim. Acta 143 (2014) 49–55.

[45] H. Wang, C. Zhang, Z. Liu, L. Wang, P. Han, H. Xu, K. Zhang, S. Dong, J. Yao, G. Cui, Nitrogen-doped graphene nanosheets with excellent lithium storage properties, J. Mater. Chem. 21 (2011) 5430.

[46] J. Zhang, B. Guo, Y. Yang, W. Shen, Y. Wang, X. Zhou, H. Wu, S. Guo, Large scale production of nanoporous graphene sheets and their application in lithium ion battery, Carbon 84 (2015) 469–478.

[47] S. Han, D. Wu, S. Li, F. Zhang, X. Feng, Porous Graphene Materials for Advanced Electrochemical Energy Storage and Conversion Devices, Adv. Mater. 26 (2014) 849–864.

[48] D. Guo, Riku Shibuya, Chisato Akiba, Shunsuke Saji, Takahiro Kondo, Junji Nakamura, Active sites of nitrogen-doped carbon materials for oxygen reduction reaction clarified using model catalysts, Science 351 (2016) 361–365.

[49] P.A. Denis, R. Faccio, A.W. Mombru, Is it possible to dope single-walled carbon nanotubes and graphene with sulfur? Chemphyschem 10 (2009) 715–722.

[50] X. Liu, Y. Wu, Z. Yang, F. Pan, X. Zhong, J. Wang, L. Gu, Y. Yu, Nitrogen-doped 3D macroporous graphene frameworks as anode for high performance lithium-ion batteries, J. Power Sources 293 (2015) 799–805.

[51] Y. Su, Y. Liu, P. Liu, D. Wu, X. Zhuang, F. Zhang, X. Feng, Compact coupled graphene and porous polyaryltriazine-derived frameworks as high performance cathodes for lithium-ion batteries, Angew. Chem. Int. Ed. Engl. 54 (2015) 1812–1816.

[52] X. Li, Y. Hu, J. Liu, A. Lushington, R. Li, X. Sun, Structurally tailored graphene nanosheets as lithium ion battery anodes: an insight to yield exceptionally high lithium storage performance, Nanoscale 5 (2013) 12607–12615.

[53] B. Yan, M. Li, X. Li, Z. Bai, L. Dong, D. Li, Electrochemical Impedance Spectroscopy Illuminating Performance Evolution of Porous Core–Shell Structured Nickel/Nickel Oxide Anode Materials, Electrochim. Acta. 164 (2015) 55–61.